Exp Fluids (2016) 57:106
DOI 10.1007/s00348-016-2190-0

RESEARCH ARTICLE

On a PLIF quantification methodology in a nonlinear dye response regime

P. Baj[1] · P. J. K. Bruce[1] · O. R. H. Buxton[1]

Received: 2 October 2015 / Revised: 14 May 2016 / Accepted: 14 May 2016
© The Author(s) 2016. This article is published with open access at Springerlink.com

Abstract A new technique of planar laser-induced fluorescence calibration is presented in this work. It accounts for a nonlinear dye response at high concentrations, an illumination light attenuation and a secondary fluorescence's influence in particular. An analytical approximation of a generic solution of the Beer–Lambert law is provided and utilized for effective concentration evaluation. These features make the technique particularly well suited for high concentration measurements, or those with a large range of concentration values, c, present (i.e. a high dynamic range of c). The method is applied to data gathered in a water flume experiment where a stream of a fluorescent dye (rhodamine 6G) was released into a grid-generated turbulent flow. Based on these results, it is shown that the illumination attenuation and the secondary fluorescence introduce a significant error into the data quantification (up to 15 and 80 %, respectively, for the case considered in this work) unless properly accounted for.

List of symbols

B	Normalized image
$\tilde{B}$	Normalized image compensated for secondary fluorescence
G	Kernel
$\hat{G}$	Confined kernel's representation
I'_a	Primary absorption
I''_a	Secondary absorption
$\hat{I}''_\mathrm{a}$	Secondary absorption within a pixel area
I_f	Energy emitted as fluorescence
$\hat{I}_\mathrm{f}$	Energy emitted as fluorescence from a pixel area
I'_f	Primary fluorescence
$\hat{I}'_\mathrm{f}$	Primary fluorescence from a pixel area
I''_f	Secondary fluorescence
$\hat{I}''_\mathrm{f}$	Secondary fluorescence from a pixel area
I_i	Illumination light energy
I'_i	Primary illumination (incident laser light)
I''_i	Secondary illumination
Q	Optical setup transfer matrix
c	Concentration level
c_b	Background concentration level
h	Camera's transfer function
n	Secondary fluorescence kernel's exponent
r	Radial coordinate
r_0	Vessel's floor radial coordinate
H	Original image
H_b	Background image
I_0	Laser pulse energy
I_a	Energy absorbed by the dye
$\hat{I}_\mathrm{a}$	Energy absorbed within a pixel area
s	Coordinate along a laser ray
x	Cartesian coordinate
y	Cartesian coordinate
Δ_G	Kernel's spatial support size
Δ	Pixel size
α	Circumferential coordinate
β	Reflection rate
χ	Primary fluorescence share in the total fluorescence
χ_b	Primary fluorescence share of the background image
δ	Dirac delta function
ϵ	Extinction coefficient
γ	Laser sheet's circumferential profile
γ^*	Normalized laser sheet's profile
ϕ^*	Tank experiment's concentration dependence profile
ϕ	Quantum yield

✉ P. Baj
p.baj@imperial.ac.uk

[1] Imperial College London, Exhibition Road, London SW7 2AZ, UK

Published online: 03 June 2016

ψ Reflection angle
ψ_c Critical reflection angle
θ Secondary fluorescence kernel's integral

1 Introduction

Laser-induced fluorescence (LIF) is a popular experimental technique for conducting concentration measurements. It consists of introducing some fluorescent tracer into the flow of interest, illuminating the dye puff with laser light and capturing the fluorescent light emitted by the dye with an optical device. LIF takes advantage of the Stokes shift, i.e. the separation between the peaks of the absorption and emission spectra of the dye in wavelength space, which allows easy discrimination between the illumination and the fluorescent light. The latter can be directly linked to the local dye concentration value and thus allows a non-intrusive concentration measurement. Different variants of LIF have been developed over the years extending its applicability from single point and line measurements to plane measurements or even volumetric cases. Two-dimensional planar laser-induced fluorescence (PLIF) is, however, the most common version of the technique (this involves illumination with a light sheet such that a two-dimensional concentration field may be captured).

There are many successful LIF applications described in the literature. The classic papers of Koochesfahani and Dimotakis (1985), Walker (1987) and Ferrier et al. (1993) discuss most of the theoretical and technical basis for LIF. More recent studies address various specific problems of the technique (e.g. a photobleaching effect Crimaldi 1997), introduce novel calibration approaches (e.g. Sarathi et al. 2012) or simply report LIF measurement results. A review by Crimaldi (2008) summarizes most of the knowledge and experience gained so far.

Although the relation between the local dye concentration and the emitted florescent light is complicated in general, most investigators benefit from its simplified version thanks to specific conditions imposed in their experiments. When the dye concentration level is relatively low and the test section is sufficiently confined, the fluorescent response is effectively a linear function of the concentration [this assumption is adopted by Walker (1987), Crimaldi (1997), Vanderwel and Tavoularis (2014) amongst others]. This might be seen as quite restrictive, especially in turbulent flows where local high concentrations may occur, despite the relatively low mean value, that would lead to a significant illumination extinction. Therefore, some more conservative approaches account for a laser light absorption as it passes through the solution which brings non-locality into the relation [these techniques are represented by Ferrier et al. (1993) or Sarathi et al. (2012)].

The technique presented in this work is the next step towards accounting for complexity of the fluorescence phenomenon. The major advancement consists in dropping the linearity assumption, i.e. the relation between the local fluorescence and the concentration level is regarded as an arbitrary nonlinear function that is to be determined in the calibration process. Secondly, a new efficient way of correcting for the light attenuation is presented. Finally, a procedure discriminating the secondary fluorescence's influence is introduced. This is of a great importance because, as shown originally by Vanderwel and Tavoularis (2014), the secondary fluorescence can account for more than 50 % of the observed fluorescent light, leading to huge measurement errors.

The motivation behind the current work was to develop an approach that would exploit the full measurement range offered by the camera utilized in a PLIF experiment. As obvious as it sounds, it might become challenging in some cases. There are certain constraints imposed on the researcher; e.g. there is a trade-off between the illumination energy density and the size of the field of view because the available energy is limited. In particular, if one aims for a large field of view, either a powerful illumination source or a highly concentrated dye solution is needed (otherwise the fluorescent response is too weak to fill the entire measurement range). The first way might be difficult to follow as it is usually associated with some hardware limitation. On the other hand, the alternative is limited by the solubility level which, however, is typically very high. Both approaches might lead to a nonlinear dye response, with respect either to the illumination intensity or to the concentration value, if certain levels are exceeded. This is where the call for accounting for the nonlinear dye response originates from. The presented calibration technique is associated with the second approach as it seems to be more flexible in general. The additional advantage is that the range of resolved concentrations can be expanded to some extent in this case. It is due to the fact that the derivative of the fluorescence intensity with respect to the concentration level decreases at high concentration values (see, e.g., Ferrier et al. 1993), lowering the measurement's resolution there (in terms of concentration).

Performance of the developed quantification procedure is presented for the case of a study on mixing in flows past multiscale obstacles (see, e.g., Laizet and Vassilicos 2012). The fluorescent dye is isokinetically released into the flow and observed as it diffuses/mixes in the wake of the obstacles. An auxiliary tank experiment is also performed as it is demanded by the calibration technique.

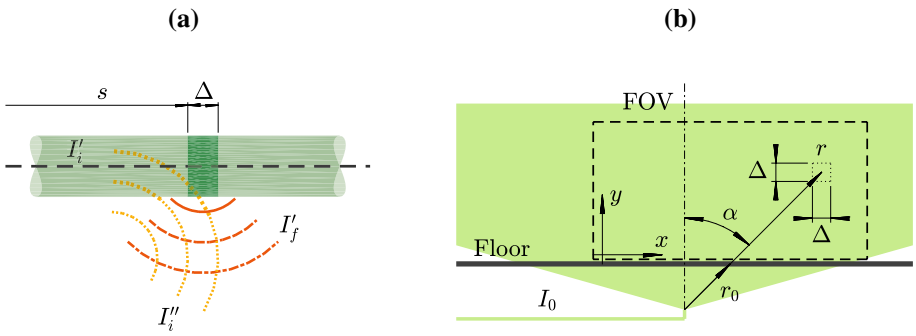

Fig. 1 **a** Schematic of a laser beam passing through a fluorescent dye solution and **b** schematic of a laser sheet passing through a tank containing fluorescent dye solution

2 The theoretical measurement model

Let us start with the theoretical model utilized in the current study. Energy I'_{i} carried by a light ray is attenuated according to the Beer–Lambert law as it passes through a fluorescent solution (see Fig. 1a for the schematic). Its spatial decay rate is dictated by the local concentration c, an energy absorption coefficient ϵ (often referred to as the extinction coefficient) and the local illumination intensity I'_{i}, as gathered by (1) (I_0 is the pulse initial energy and s is a coordinate along the ray's path).

$$\begin{aligned} \mathrm{d}I'_{\mathrm{i}} &= -\epsilon c(s) I'_{\mathrm{i}}(s)\mathrm{d}s \\ I'_{\mathrm{i}}(s) &= I_0 \exp\left(-\epsilon \int_0^s c(\zeta)\,\mathrm{d}\zeta\right) \end{aligned} \tag{1}$$

The energy deficit is absorbed by the dye molecules causing their transitions from a ground state to an excited state which then trigger a fluorescent emission. It used to be assumed implicitly by researchers in the past (e.g. Walker 1987; Crimaldi 2008) that the incident laser light I'_{i} is the only important source of the dye excitation; however, some recent results by Vanderwel and Tavoularis (2014) suggest that secondary illumination effects should also be considered. As the aforementioned work is the very first approach to the problem there are no models available in the literature that could fit into the case considered by this study, which is our present motivation.

Let us postulate that the total energy absorbed by the dye, which shall be denoted by I_{a}, is composed of two parts, i.e. I'_{a} and I''_{a}, that are due to the primary illumination I'_{i} (the incident laser light) and a secondary illumination I''_{i} (caused by fluorescent light induced by I'_{i}), respectively. The second component introduces non-locality into the problem as I'_{i} induces fluorescence everywhere within the field and all of this light contributes to I''_{i} at a considered point. Equation (2) expresses this in both differential and integral forms (throughout the text symbols with hats designate an integration over a small interrogation volume, typically over a single pixel whose size is denoted by Δ):

$$\begin{aligned} \mathrm{d}I_{\mathrm{a}} &= \mathrm{d}I'_{\mathrm{a}} + \mathrm{d}I''_{\mathrm{a}} = -\mathrm{d}I'_{\mathrm{i}} + \epsilon c(s) I''_{\mathrm{i}}(s)\mathrm{d}s \\ \hat{I}_{\mathrm{a}}(s) &= \int_{s-\Delta/2}^{s+\Delta/2} \mathrm{d}I_{\mathrm{a}} \simeq \epsilon \Delta c(s) I'_{\mathrm{i}}(s) + \hat{I}''_{\mathrm{a}}(s) \end{aligned} \tag{2}$$

The absorbed energy is partially reemitted as fluorescent light $\hat{I}_{\mathrm{f}}$ with a ratio between absorbed and emitted photons, the quantum efficiency, denoted here by ϕ, which is a function of the local concentration. Thus, the fluorescent light's energy emitted by the dye can be expressed as (3) (the primary and secondary illumination contributions to the emission are denoted by $\hat{I}'_{\mathrm{f}}$ and $\hat{I}''_{\mathrm{f}}$, respectively).

$$\begin{aligned} \hat{I}_{\mathrm{f}}(s) &= \phi\big(c(s)\big)\hat{I}_{\mathrm{a}}(s) = \hat{I}'_{\mathrm{f}}(s) + \hat{I}''_{\mathrm{f}}(s) \\ &= \epsilon \Delta c(s) \phi\big(c(s)\big) I'_{\mathrm{i}}(s) + \hat{I}''_{\mathrm{f}}(s) \end{aligned} \tag{3}$$

The secondary fluorescence is the result of an additional excitation being imposed in addition to the laser light, that is itself laser-induced fluorescence. One can even consider an infinite feedback loop (the secondary fluorescence triggers a third level of fluorescence, etc.), but for simplicity the entire effect is collapsed into $\hat{I}''_{\mathrm{f}}$ in this paper. The secondary fluorescence induced at one point by the primary fluorescence emitted at another should decrease with an increasing separation between them, roughly as a power law because the sphere's surface into which the light is radiated grows parabolically. Therefore, it is proposed to model the secondary fluorescence as a convolution of the primary fluorescence with a kernel G that exhibits a power law decay as given by (4). Although some additional effects, like the light attenuation or the contribution from light scattered by PIV particles, can cause deviation from this trend, they are also accounted for by (4) via the adjustable kernel's parameters n and θ.

$$\begin{aligned} \hat{I}''_{\mathrm{f}}(s) &= \hat{I}'_{\mathrm{f}}(s) * G(s) \\ G(s) &= \begin{cases} \theta & |s| \le \Delta \\ \theta\left(\frac{\Delta}{|s|}\right)^n & \Delta < |s| \end{cases} \end{aligned} \tag{4}$$

By substituting (4) in (3), one can get a relation between the overall fluorescence and the primary fluorescence (5)

(δ stands for the Dirac delta function). The χ field, that appears in the equation, denotes the share of the primary fluorescence in the overall fluorescence, which shall be a convenient measure of the considered phenomenon's magnitude.

$$\hat{I}_{\mathrm{f}}(s) = \hat{I}'_{\mathrm{f}}(s) * \big(\delta(s) + G(s)\big) = \frac{\epsilon \Delta c(s) \phi\big(c(s)\big)}{\chi(s)} I'_{\mathrm{i}}(s)$$
$$\chi(s) = \frac{\hat{I}'_{\mathrm{f}}(s)}{\hat{I}_{\mathrm{f}}(s)} \tag{5}$$

A similar expression can be written for a laser sheet, as it can be seen as a grouping of adjacent rays. Let's assume that the laser sheet's virtual origin is aligned with an origin of the polar system (r, α) (see Fig. 1b for the schematic) and that the laser sheet first crosses the dye at a certain radial position denoted by r_0 (which can be a function of α in general). The primary illumination energy received by a single pixel can be approximated by (6) (given $r_0 \gg \Delta$ so that the polar grid lines can be considered locally parallel), where γ stands for the laser sheet's circumferential profile. The corresponding fluorescence energy is given by (7).

$$I'_{\mathrm{i}}(r, \alpha) = I_0 \frac{\Delta}{r} \gamma(\alpha) \exp\Big(-\epsilon \int_{r_0}^{r} c(\zeta, \alpha)\, \mathrm{d}\zeta \Big) \tag{6}$$

$$\hat{I}_{\mathrm{f}}(r, \alpha) = \frac{\epsilon \Delta c(r, \alpha) \phi\big(c(r, \alpha)\big)}{\chi(r, \alpha)} I'_{\mathrm{i}}(r, \alpha) \tag{7}$$

In a standard PLIF experiment $\hat{I}_{\mathrm{f}}$ is measured by a camera located in front of the laser sheet. However, what is actually seen by the camera is a small fraction of $\hat{I}_{\mathrm{f}}$ that is directed towards the collecting optics and further spatially modulated by, e.g., lens' imperfections, the channel's side wall glass' properties (let us collapse all these effects, that are setup specific, into a transfer matrix Q). Additionally, since the whole volume is excited by the secondary illumination, emission along the entire line of sight attributes to the pixel count rather than in-sheet radiation only, as pointed out by Vanderwel and Tavoularis (2014). Finally, the camera output H can be affected by the camera's transfer function h deviating from linearity. The summarized fluorescence model utilized in this study is thus given by (8).

$$H(r, \alpha) = h\Big(I_0 \frac{\epsilon \Delta^2 \gamma(\alpha) Q(r, \alpha) c(r, \alpha) \phi\big(c(r\alpha)\big)}{r \chi(r, \alpha)} \exp\Big(-\epsilon \int_{r_0}^{r} c(\zeta, \alpha)\, \mathrm{d}\zeta \Big) \Big) \tag{8}$$

3 Experimental setup

This work was carried out in the hydrodynamic laboratory of the Department of Aeronautics at Imperial College London. Two separate PLIF experiments were conducted: a main experiment utilizing a recirculating open water channel facility (having a cross section of 0.6 × 0.6 m and a measurement length of 8.0 m) and a calibration measurement that was run in a small tank of 350 × 250 × 400 mm size. The same optical setup was used in both cases; however, two additional cameras were added in the main experiment for simultaneous particle image velocimetry (PIV) measurements.

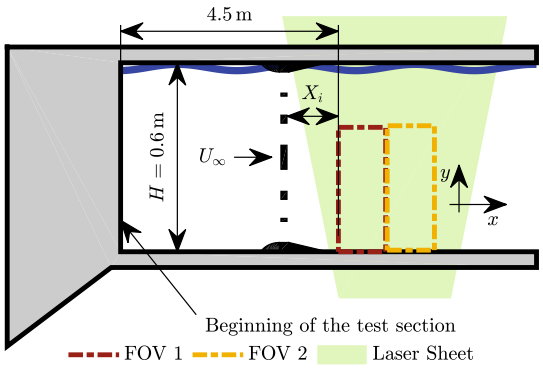

Fig. 2 Main experimental setup

Table 1 Initial concentration of the dye, measured with 2 % tolerance, released at different downstream stations (X_{i})

	X_1	X_2	X_3	X_4
x (mm)	0	450	900	1350
c_0 (μmol l^{-1})	207	597	1145	2053

3.1 The main experiment

The main experiment consisted of tracking a diffusing passive tracer, i.e. rhodamine 6G dye, after it was isokinetically released into the turbulent flow from a point source located in the near wake of a multiscale turbulence generator. The mean velocity was set to 0.2 m s^{-1} which corresponded to a cross section-based Reynolds number of 120,000. A schematic diagram of the setup is given in Fig. 2.

The mid-plane of the flow was illuminated with the laser light. Two cameras in a side by side arrangement, located in front of the laser sheet, produced an extended stitched field of view of 390 × 450 mm (with 0.15 mm spatial resolution) as presented in Fig. 2. The turbulence generator was traversed in the streamwise direction in order to capture different downstream positions of the flow (in that way the positions of the cameras and optics were fixed throughout the experiment). Four different stations were examined and the initial concentrations of the dye released at each of them are summarized in Table 1 (in each case the release rate equalled 50 μl s^{-1}).

The experiment was held in a recirculating, closed-loop water channel which, as a result, led to a certain residual level of the dye being present in the flume throughout the experiment. The water was changed frequently in order to keep this background concentration below a certain level. As a single acquisition's time was small compared to the full recirculation time, it is possible to assume that the residual concentration was constant during a single experiment's run. In order to account for this phenomenon a set of background images was taken before every acquisition.

3.2 The tank experiment

The auxiliary calibration experiment was performed beforehand in a small transparent tank. Just like in the main experiment, the entire optical setup was fixed. The tank was filled with a uniform dye solution and placed in the flume at the exact position of the cameras' fields of view. In order to ensure the optical path's properties are preserved (i.e. that a light ray enters the water at exactly the same position in both experiments), the flume was filled with water to the same level. Sets of images were acquired for 20 different concentration levels ranging between $0.06 - 1.73\,\mu\mathrm{mol\,lt}^{-1}$. The amount of dissolved dye was measured with 3 % tolerance.

3.3 The dye

Rhodamine 6G was chosen as the fluorescent dye for the purpose of this study (CAS: 989-38-8, 95 % purity, Sigma-Aldrich Company Ltd). Its molar mass equals $479\,\mathrm{g\,mol}^{-1}$, and its water solubility reaches $20\,\mathrm{g\,l}^{-1}$. The Schmidt number (the ratio between viscous diffusion rate and molecular diffusion rate) data available in the literature is highly scattered; however, a value of 2500 is cited most frequently (e.g. Gendron et al. 2008; Vanderwel and Tavoularis 2014). The emission and absorption spectra, as presented by Sarathi et al. (2012), are plotted in Fig. 3. The exact positions of the peaks may vary with different parameters (e.g. Bindhu et al. (1999) reports a concentration dependence); however, the changes are of a negligible order.

Rhodamine 6G is quite popular as a PLIF tracer thanks to its specific properties. Its absorption peak that occurs at 525 nm makes almost an exact match with the second harmonic of Nd:YLF laser light (527 nm), but it is also well suited for the Nd:YAG case (532 nm). The quantum efficiency is relatively high and within a wide range of concentration levels (given a sufficient solution purity) stays above 0.9 (see Penzkofer and Leupacher 1987 for reference). Effects of *pH* and temperature are known to be negligible (see Zhu and Mullins 1992), and the dye is highly resistant to photobleaching as proven by Crimaldi (1997). All these reasons, therefore, make it a good choice for a concentration measurement.

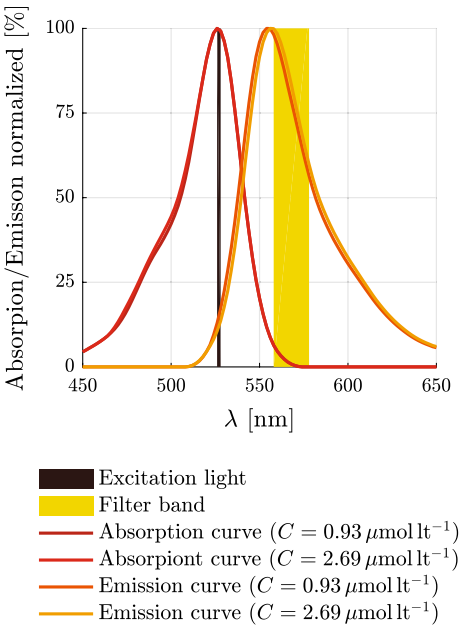

Fig. 3 Rhodamine 6G emission and absorption spectra normalized with the peak values (following Sarathi et al. 2012)

3.4 Instrumentation

A Litron LDY304 Nd:YLF laser, running at 240 Hz frequency, was used as the illumination source throughout the course of these measurements. It provided 25 mJ of energy per shot with a standard deviation of roughly 0.5 %, which was quantified with a LabMax-TOP energy meter fitted with a J-50MT sensor (both manufactured by Coherent Inc.). A divergent laser sheet, having a full width at half maximum below 1.0 mm at its waist, was formed in the experimental zone by means of a setup of mirrors, lenses and a pinhole. The instantaneous illumination power density was estimated to be below $0.4\,\mathrm{GW\,m}^{-1}$ everywhere within the laser sheet. Such a value guarantees reasonable linearity of the fluorescent response to the illumination (see Shan et al. 2004 for details). This was further confirmed in some preliminary studies.

Two Vision Research Phantom v641 cameras having 105 mm *f*/2 Nikkor lenses attached and providing 12-bit images with 2560×1600 pix resolution were utilized in the experiment. Each was fitted with an additional optical filter, whose band is centred at 568 nm and spans over 20 nm, to discriminate between fluorescent and laser light (see Fig. 3). The cameras are optimized for the main experiment, i.e. the *f* number of the downstream camera's lens is decreased to account for the lower expected concentration values. An adverse effect of this is that it saturates at comparatively smaller concentration values in the tank experiment. The camera's quantum efficiency is quite uniform within the filter's band and equals 0.58.

A Bürkert Micro Dosing Unit 7615 was adopted for the dye releasing system. It allows a precise dosing (5 µl level) at a frequency up to 40 Hz. In order to even out the discrete dye releasing manner a long elastic piping (2 m) was attached between the dosing unit and the dye releasing point. It was confirmed in the PIV results that the dye was introduced isokinetically into the flow (i.e. no differences in the velocity field were spotted between the unit being switched on or off cases).

4 The quantification procedure

As indicated in Sect. 2, the proposed quantification technique utilizes (8) as a general relation linking an acquired image H and the underlying concentration field c. Before proceeding further let us highlight some general assumptions that apply throughout the study:

- A dark image (the image taken with a closed shutter) is subtracted from all the measurements beforehand to ensure $h(0) = 0$.
- The optical setup's transfer function Q, the camera's transfer function h and the laser sheet's circumferential profile γ are time-invariant parameters of the particular measurement setup.
- The extinction coefficient ϵ is a constant specific to the experimental conditions (e.g. water purity), and no concentration dependence exists in particular (Selwyn and Steinfeld (1972) reports 5 % change over a range 0.8–80 µmol l^{-1}, which is much broader than the range considered in this work).
- The quantum yield ϕ is an arbitrary function of concentration, specific to the experimental conditions.
- The primary fluorescence share χ depends on the c field's topology, not on its scale.

$$B(r,\alpha) = \frac{h^{-1}\big(H(r,\alpha)\big)}{h^{-1}\big(H_\mathrm{b}(r,\alpha)\big)} = \frac{\chi(r,\alpha)c(r,\alpha)\phi\big(c(r,\alpha)\big)}{\chi_\mathrm{b}(r,\alpha)c_\mathrm{b}\phi(c_\mathrm{b})} \times \exp\Big(-\epsilon\int_{r_0}^{r}\big(c(\zeta,\alpha)-c_\mathrm{b}\big)\,\mathrm{d}\zeta\Big) \tag{9}$$

Given the above, it is possible to rearrange the quantification problem by taking advantage of the background concentration images that are acquired before each experiment's run (they are referred to as H_b). By defining a normalized image B, see (9), one removes Q and γ from the problem, which comes at the cost of introducing an additional unknown field χ_b (the primary fluorescence share of the background image) and an unknown scalar c_b (the background concentration level). Equation (9) employs two groups of unknowns: ones that are inherent to a particular acquisition, e.g. the c field, and those that are shared between all the measurements utilizing the same setup, i.e. the functions ϕ and h and the coefficient ϵ. It is, therefore, worth decoupling the problem to evaluate the second group of unknowns beforehand, in the auxiliary tank experiment, where one can explicitly impose the concentration field.

4.1 The tank experiment

As stated above, the purpose of the tank experiment is to establish the camera's transfer function h, the quantum yield function ϕ and the extinction coefficient ϵ. To do so, several sets of images of the tank filled with a homogeneous dye solution were captured, each for a different concentration value. Unlike in the main experiment, the background concentration images are not available (as there is no background concentration for the tank experiment) so it is necessary to utilize formulation (8) in this case.

Following Vanderwel and Tavoularis (2014), who considered an almost identical setup, it is presumed that χ is a constant in the tank experiment, which implies proportionality between the primary and the secondary fluorescence fields. This assumption is not in line with the theoretical model of secondary fluorescence postulated in Sect. 2; however, these two approximations approach each other in the limit of an uniform primary fluorescence field. It is not exactly the case for the tank experiment (i.e. the density of illumination energy varies in space, there are side walls limiting the field); however, as shown in the referenced work, this approach still provides a decent approximation. After adopting the aforementioned condition the equation takes the simplified form of (10). It follows that the tank calibration images are exactly determined by the quantities that are to be evaluated plus the laser sheet's profile γ.

$$H(r,\alpha) = h\Big(\mathrm{Const}\cdot Q(r,\alpha)\frac{\epsilon\gamma(\alpha)c\phi(c)}{r}\exp\big(-\epsilon c(r-r_0)\big)\Big) \tag{10}$$

4.1.1 The camera's transfer function, h

Let us first consider a single pixel row of data acquired in the tank experiment very close to the floor (i.e. $H(r_0,\alpha)$). The attenuation can be neglected at this position since the light has not travelled far enough yet to be considerably altered. Further, let us assume that h is a linear function at high values of its argument (the captured light intensity). One can try to express $H(r_0,\alpha)$ as a product of two independent functions ϕ^* and γ^*, where the former depends only on c and the latter represents purely α dependence, which is given by (11). It follows from the linearity assumption that this representation should hold at least at

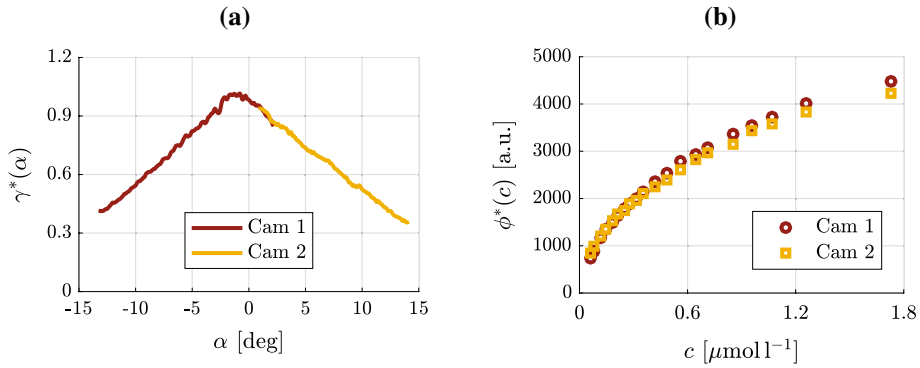

Fig. 4 **a** The α dependent profile γ^* and **b** the c dependent profile ϕ^*

high values of the transfer function's arguments. Note that in such case $\phi^* \sim c\phi$ and $\gamma^* \sim Q\gamma$, which means both ϕ^* and γ^* can be easily approximated. Firstly, let us assign $H(r_0, \alpha)$ acquired at the highest concentration to γ^*. This maximizes the chances that γ^* is defined within the linear range (high concentration value translates to high energy received by the camera) and is also beneficial from a signal-to-noise ratio perspective. Additionally, in order to fully define both γ^* and ϕ^*, let's postulate that the former is further normalized with its peak value. Next, one can approximate ϕ^* as the peak value of $H(r_0, \alpha)$ for a given concentration level. The resulting curves, reasonably collapsed for both cameras, are depicted in Fig. 4.

$$H(r_0, \alpha) = h\big(\text{Const} \cdot Q(r_0, \alpha) c\phi(c)\gamma(\alpha)\big) \simeq \phi^*(c)\gamma^*(\alpha) \tag{11}$$

A range of validity of the representation given by (11) can be examined by calculating a ratio between the actual value of $H(r_0, \alpha)$ and the one approximated by the proposed expression, i.e. $\phi^*\gamma^*$ (the ratio should oscillate around 1 in the ideal case). The result of such an attempt, presented in Fig. 5, confirms that the approximation (11) holds but only in a limited domain, i.e. for either high c values or α values close to 0. It follows from the shapes of γ^* and ϕ^* that this area corresponds to a relatively high value of the product of these two, which is equivalent to a high intensity of the fluorescent light. This behaviour strongly indicates that the function h departs from linearity at small values of the captured light's intensity. Note that some blank areas appear in the figure due to local saturations. This effect is particularly pronounced for the second camera, as the f number of its respective lens was comparably smaller (see Sect. 3). Nevertheless, the data obtained from the non-saturated parts of the images are valid.

Regardless of the actual shape of h at low illumination values, $\phi^*\gamma^*$ stays proportional to the transfer function's argument everywhere in the domain as long as both ϕ^* and γ^* are evaluated in the linear range of h. Therefore, by plotting $\phi^*\gamma^*$ vs. $H(r_0, \alpha)$, one can reveal the function h (with respect to its magnitude). Instead, for clarity reasons, let us consider a ratio between the transfer function

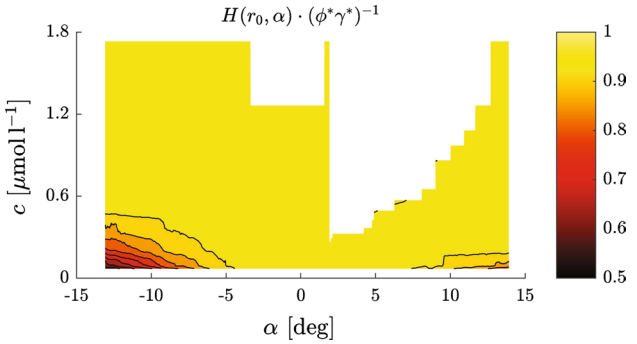

Fig. 5 $H(r_0, \alpha)$ profiles' collapse (the *white* spots correspond to camera saturation)

and its argument (which does not alter the generality of the approach). The corresponding set of curves can be obtained by plotting $\phi^*\gamma^*$ vs. $H(r_0, \alpha) \cdot (\phi^*\gamma^*)^{-1}$ for different concentration levels. It follows from the logic outlined above that they should collapse onto a single curve, which, in particular, should form a horizontal line within the linearity range of h. What is presented in Fig. 6a, however, does not exactly coincide with this scenario, i.e. a considerable scatter of the curves is very clear. On the other hand, there is a distinguishable plateau at the high values of $\phi^*\gamma^*$, which is well collapsed. It is important to note that, since the curve corresponding to the highest considered concentration (i.e. the brightest one in Fig. 6a) is located entirely within the plateau area where the linearity assumption holds, the γ^* approximation is valid. It is not the case for ϕ^*, as peaks of the curves affiliated to the remaining concentration levels do not necessarily fulfil this condition, especially for the lowest c values. Therefore, the observed scatter appears as an effect of the wrong approximation of ϕ^* at low c values.

$$\phi^*_{\text{cor}} = \phi^* \cdot \left(1 + \frac{a_1}{(c + a_2)^{a_3}}\right) \tag{12}$$

If one was able to find a correction to ϕ^* that results in the collapse of all the lines, the true evolution of h would be established. Although the exact shape of h is unique,

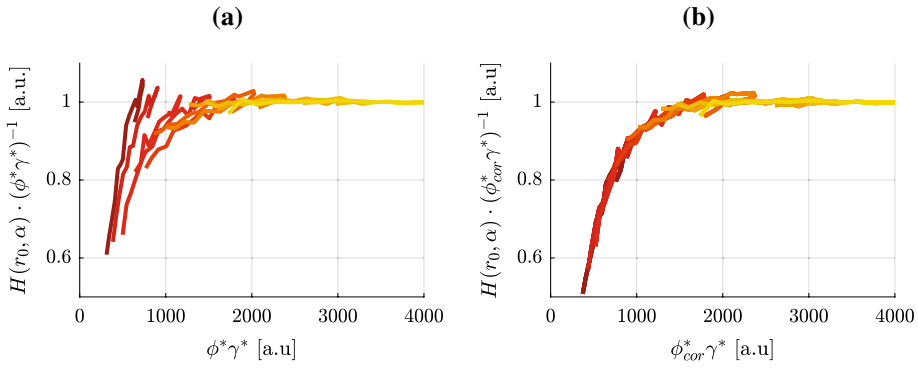

Fig. 6 $H(r_0,\alpha)\cdot(\phi^*\gamma^*)^{-1}$ profiles collapse **a** before and **b** after (12) correction is applied (the affiliated c value changes from *dark to bright colours* within the range 0.06–1.73 μmol l^{-1})

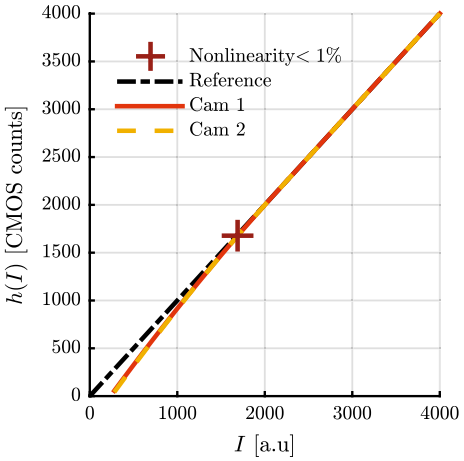

Fig. 7 Cameras' transfer functions (the *cross* indicates the position of 1 % deviation from the reference linear law)

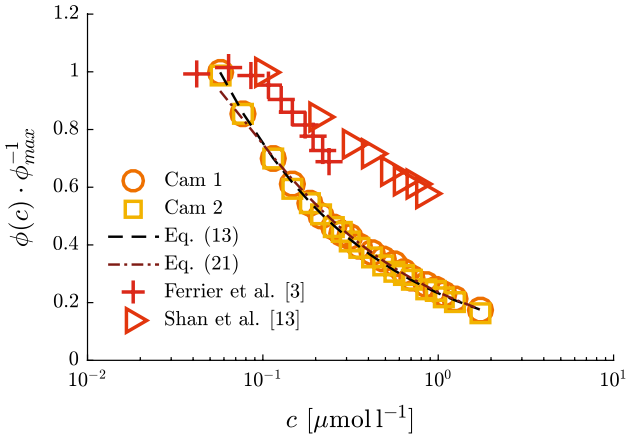

Fig. 8 Normalized quantum yield functions (data gathered in the current study and recovered from the literature)

there are many possible correction formulations that are able to approximate it, providing a reasonable collapse. Let us, therefore, arbitrarily pick one of them that is gathered by (12) (ϕ^*_{cor} stands for the compensated ϕ^* and a_k are fit parameters evaluated in an iterative procedure that maximizes an arbitrary collapse measure). A satisfactory level of overlap is achieved, as presented in Fig. 6b. The resulting cameras' transfer functions h are subsequently plotted in Fig. 7 along with a reference line. For both cameras, whose functions collapse almost perfectly, a nonlinearity exceeding 1 % (a deviation from the reference line) is observed for read-outs below 1680CMOS counts and more than 10 % divergence is seen under 960CMOS counts (this translates to 41 and 23 % of a 12-bit image saturation, respectively).

4.1.2 The quantum efficiency, ϕ

After the proper transfer function h is found, it is possible to use (11) to evaluate ϕ. Unfortunately, the exact magnitude is not available, as a value for the constant present in (11) is unknown and neither are the exact forms of Q and γ. Nevertheless, it is enough for the purpose of solving (9), because the magnitude of ϕ is divided out from this equation.

$$\phi\cdot{\phi_{\max}}^{-1}\simeq a_1 c^{a_2} \tag{13}$$

$\phi\cdot{\phi_{\max}}^{-1}$ is evaluated (where $\phi_{\max}=\max\phi$) via a least square fit into $h^{-1}\big(H(r_0,\alpha)\big)$ for different α value. Note that the dependence on the unknown quantities is now lost due to the applied normalization. The result is plotted in Fig. 8 along with data from the literature. Curves for both cameras are well collapsed and can be fairly approximated with a power law (13) (where the fit parameters a_k are equal to 0.233 and −0.509, respectively); however, the decay starts quite early compared to the literature. Several factors may contribute to this, e.g. different water and dye purity (different substances may promote quenching and decrease the quantum yield, see Penzkofer and Lu (1986) for reference) or the use of a different filter [the quenching might be stronger at certain wavelengths, see Penzkofer and Leupacher (1987)]; however, it is impossible to say what the exact reason is. Regardless, the collapse suggests

Table 2 Values of the extinction coefficient reported in the literature

Previous works	ϵ [l (mm mol)$^{-1}$]
Selwyn and Steinfeld (1972)	7000
Walker (1987)	8510
Hannoun and List (1988)	14,400
Ferrier et al. (1993)	11,000
Deusch and Dracos (2001)	11,600

that the behaviour is physical and all the following results are based on these calibration curves. The discussed results well illustrate the need to account for the variation of the quantum yield in our study as opposed to assuming its constancy across a certain range of c values, which is usually done in the literature (e.g. Ferrier et al. 1993).

4.1.3 Extinction coefficient estimation, ϵ

The next step of the calibration procedure is to evaluate the extinction coefficient. Let us consider (10) once more for this purpose. By moving some terms to the left-hand side of the equation and evaluating its logarithm, one arrives at (14). Further, by calculating derivatives of both sides with respect to c, an explicit formula for ϵ is reached. Note that the dependence on all the unknown quantities (e.g. Q) is thereby conveniently lost.

$$\log\left(\frac{h^{-1}\big(H(r,\alpha)\big)\phi_{\max}}{c\phi(c)}\right) = \log\left(\text{Const}\cdot Q(r,\alpha)\frac{\epsilon\gamma(\alpha)\phi_{\max}}{r}\right) - \epsilon c(r-r_0)$$

$$\epsilon = -\frac{1}{r-r_0}\frac{\partial}{\partial c}\log\left(\frac{h^{-1}\big(H(r,\alpha)\big)\phi_{\max}}{c\phi(c)}\right) \tag{14}$$

Equation (14) allows evaluation of ϵ at each (r,α) point. However, only measurements at different α positions are fully independent as these are taken along different light rays. Additionally, the estimate's quality should improve with a growing radial coordinate as the attenuation becomes more pronounced, translating into a better signal-to-noise ratio. Therefore, only data from the upper half of the tank will be considered in this analysis.

The ϵ measurements' probability density function (PDF) is presented in Fig. 9. Although the data are quite spread (the 95 % confidence intervals' span over 12001 (mm mol)$^{-1}$, roughly), clear peaks exist (54201 (mm mol)$^{-1}$ and 55001 (mm mol)$^{-1}$ for camera 1 and camera 2, respectively) and the difference between them is well within the uncertainty. The values are smaller compared to those seen in the literature, as summarized in Table 2; however, the difference is not significant compared to the data's scatter.

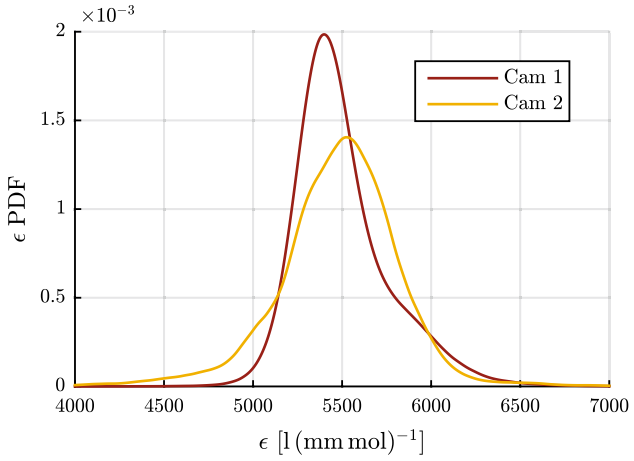

Fig. 9 Extinction coefficient measurements' distribution

4.1.4 Residual of the calibration

As stated in the beginning of this section, it should be possible to collapse the tank calibration images with the quantities established so far. Equivalently, one should be able to reconstruct the acquired images by the following (10). It is worth checking the residual of the reconstruction to get an idea of the calibration's quality.

Let the reconstructed images be denoted by H_{rec}. As shown in Fig. 10, H_{rec} closely follows the corresponding H images. The ratio of these two, which should ideally be equal to 1, varies to within ± 10 %. It is worth noting, however, that the same pattern appears in the case of each concentration level. This most certainly has to do with the fact that the optic's transfer function Q is non-uniform. Let us therefore account for this by subtracting the mean pattern (averaged across all the considered concentration levels) from the residual images. This leads to rather uniform final residuals. The associated standard deviations are below 3 % for all the concentrations, which is a rather satisfactory level, and no distinctive spatial patterns exist apart from aligning the values with laser rays which might be easily explained by, e.g., dust redistribution during the measurement.

4.2 Secondary fluorescence correction

The secondary fluorescence, as described by Vanderwel and Tavoularis (2014), can account for a considerable amount of the overall fluorescence. An empirical correlation between the width of a tank W and percentage share of secondary fluorescence is provided in the referenced paper, which can be expressed as (15) if the laser sheet is aligned with a central plane of the tank (σ stands for the light sheet thickness). For the tank experiment case considered in this

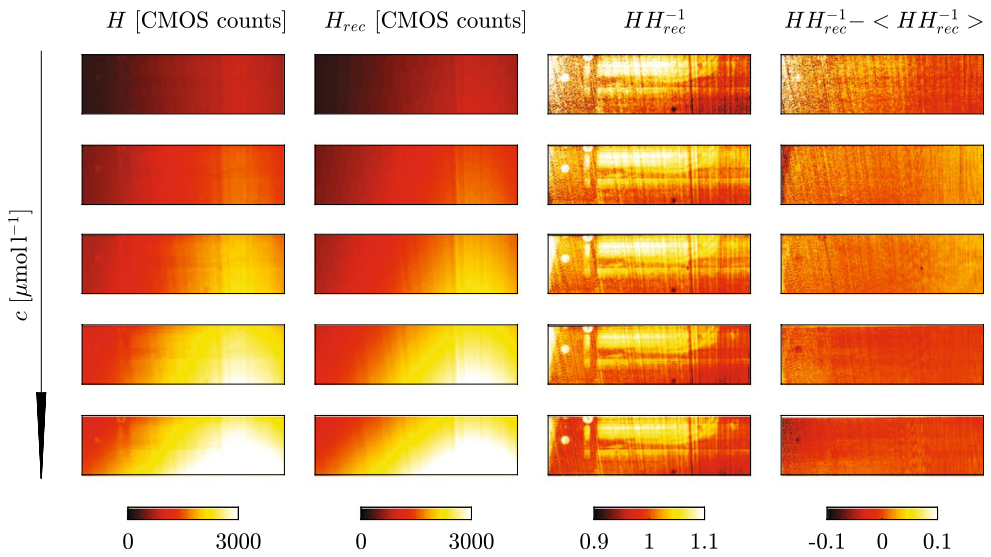

Fig. 10 *Columns* from *left to right* original images, calibration-based reconstructions, residual fields, residual fields after the mean pattern subtraction

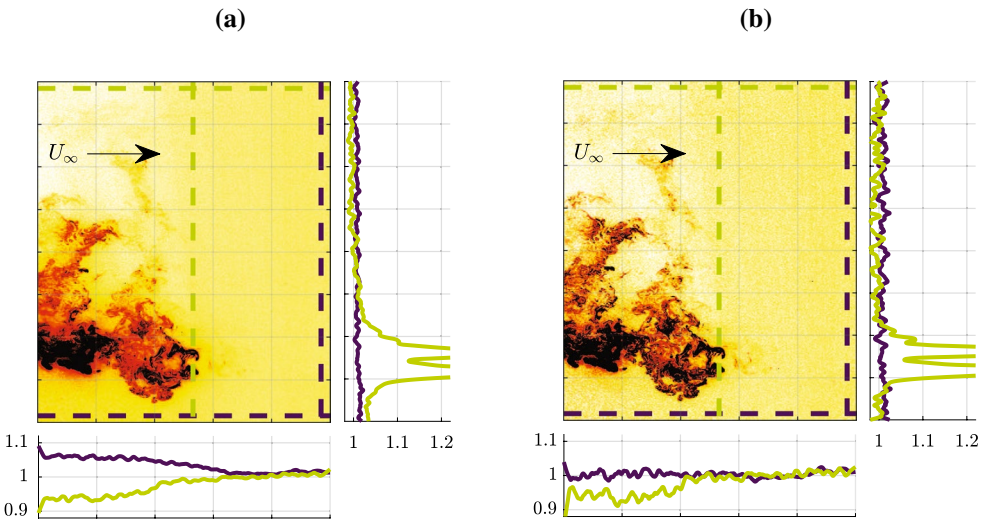

Fig. 11 **a** An example normalized image B [see (9)] and **b** the associated compensated image $\tilde{B}$ [see (18)]; side plots are the profiles taken along the corresponding paths

work, it returns a value of 47 %. This means it is roughly equal to the primary fluorescence. It is not possible to assess the effect of secondary fluorescence in the main experiment in the same manner because the conditions are much different (e.g. non-uniform concentration field); however, it is straight forward to show that this effect exists.

$$1 - \chi = \frac{0.33W^{0.20}}{\sigma^{0.20} + 0.33W^{0.20}} \tag{15}$$

Let us consider an instantaneous image taken at an early stage of a main experiment's run when the dye has not yet arrived at the end of the field of view. An example is presented in Fig. 11. As the experiment has just started it is reasonable to expect that the concentration level is equal to the background everywhere except for the dye puff. Contrastingly, a clear decrease is observed along the horizontal section taken below the puff (in the sense of the rays' travel) as the distance from the dye's bulk increases (a plateau is reached eventually at a value of 1). Unlike the other horizontal profile's variation, which could be linked to the laser light attenuation (this section is located above the puff), it can only be explained via the secondary fluorescence. The vertical section taken in the middle of the field of view contains two major peaks, that are far out of scale of the plot, but more importantly it presents a very mild and smooth transition from the peak to the uniform background that lasts for a considerable distance. Again, this seems to be driven by the secondary fluorescence because molecular diffusion, the other phenomenon that could be

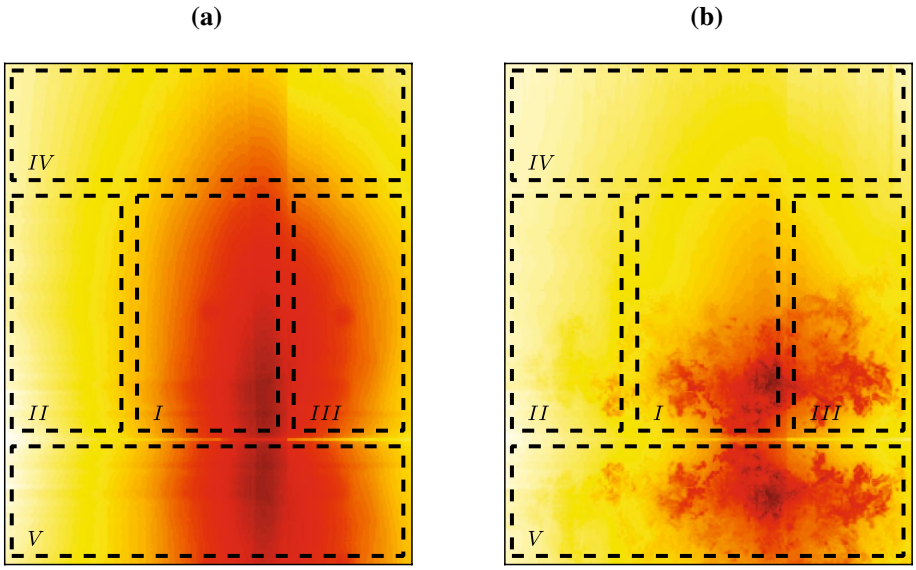

Fig. 12 Extended images: **a** the background image case, **b** the flow image case (expansion strategy for all the zones is summarized in Table 3)

potentially responsible for smoothing sharp peaks, is far too weak to develop such large structures (the Schmidt number is approximately equal to 2500).

The observation stated above forms the basis for the subsequent secondary fluorescence quantification technique. Equations (16) and (17) (considered here in Cartesian coordinates for simplicity) that come directly from (4), (7) and (8) provide a solution for the primary fluorescence $\hat{I}'_{\mathrm{f}}$ based on the convolution theorem ($\mathcal{F}$ stands for the Fourier transform and $\hat{G}$ denotes a finite representation of the kernel G, having a spatial expanse designated by Δ_G). Once $\hat{I}'_{\mathrm{f}}$ is known, it is possible to define a compensated normalized image $\tilde{B}$ [see (18)], which is much like B [see (9)] except the secondary fluorescence effect is now removed. Therefore, $\tilde{B}$ profiles should exhibit rapid drop-offs and extended plateaus in all the spots where the aforementioned intuition applies, because the smoothing effect is removed along with the secondary fluorescence. There are a number of such profiles in a typical sequence of acquired PLIF images, and thus, it is possible to set an optimization procedure for the kernel parameters that would impose this behaviour.

$$\begin{aligned} h^{-1}\big(H(x,y)\big) &= Q(x,y)\hat{I}'_{\mathrm{f}}(x,y) * \big(\delta(x,y) + \hat{G}(x,y)\big) \\ &\simeq \mathrm{Const}\cdot \hat{I}'_{\mathrm{f}}(x,y) * \big(\delta(x,y) + \hat{G}(x,y)\big) \\ \mathrm{Const}\cdot \hat{I}'_{\mathrm{f}}(x,y) &= \mathcal{F}^{-1}\left\{ \frac{\mathcal{F}\big\{h^{-1}\big(H(x,y)\big)\big\}}{\mathcal{F}\big\{\delta(x,y) + \hat{G}(x,y)\big\}} \right\} \end{aligned} \tag{16}$$

$$\hat{G}(x,y) = \begin{cases} \theta J^{-1} & \zeta \le \Delta \\ \theta J^{-1}\left(\frac{\Delta}{\zeta}\right)^n & \Delta < \zeta < \Delta_G \\ 0 & \Delta_G < \zeta \end{cases}$$

$$J = \pi\Delta^2 + \int_{\Delta}^{\Delta_G} 2\pi\zeta\left(\frac{\Delta}{\zeta}\right)^n \mathrm{d}\zeta, \qquad \zeta = \sqrt{x^2+y^2} \tag{17}$$

$$\begin{aligned} \tilde{B}(r,\alpha) &= \mathcal{F}^{-1}\left\{ \frac{\mathcal{F}\big\{h^{-1}\big(H(x,y)\big)\big\}}{\mathcal{F}\big\{\delta(x,y) + \hat{G}(x,y)\big\}} \right\}\cdot \\ &\quad \times \left(\mathcal{F}^{-1}\left\{ \frac{\mathcal{F}\big\{h^{-1}\big(H_{\mathrm{b}}(x,y)\big)\big\}}{\mathcal{F}\big\{\delta(x,y) + \hat{G}(x,y)\big\}} \right\}\right)^{-1} \\ &\simeq \frac{c(r,\alpha)\phi\big(c(r,\alpha)\big)}{c_{\mathrm{b}}\phi(c_{\mathrm{b}})} \exp\Big(-\epsilon \int_{r_0}^{r} \big(c(\zeta,\alpha) - c_{\mathrm{b}}\big)\,\mathrm{d}\zeta \Big) \end{aligned} \tag{18}$$

Although Eq. (16) provides an explicit formula for $\hat{I}'_{\mathrm{f}}$, it is not straight forward to apply because the kernel's spatial expanse Δ_G may be significant, i.e. comparable to the field of view [the kernel's numerical representation is defined by (17)], or, in other words, information reaching beyond the field of view is required to perform the deconvolutions. It is therefore crucial to expand the image by adding a margin of half of the kernel's support size at each side. Let us consider the extended image being split into five distinct zones, as presented in Fig. 12, where the middle one (zone I) corresponds to the original image. It is proposed to fill the side zones by using linear extrapolation and information from the other camera (zones *II*&*III*, respectively, this gets reversed if the other camera is considered) in the case of background images (Fig. 12a) and images taken at previous/following time steps, space-shifted according to the Taylor's hypothesis, in the flow images' case (Fig. 12b, zones *II*&*III*). Zone IV, in both cases, can be treated with a linear extrapolation while "a mirror condition" should be applied to the lower zone V, i.e. the floor reflection effect should be mimicked. This assignment is summarized in Table 3.

Close attention needs to be paid to the mirror expansion in zone V. Let us first describe the underlying physics that

Table 3 Expansion strategies assigned to the different zones of Fig. 12

Zone	Background image	Flow image
I	Original image (first camera)	Original image
II	Linear extrapolation	Taylor's hypothesis
III	Original image (second camera)	Taylor's hypothesis
IV	Linear extrapolation	Linear extrapolation
V	Mirror expansion	Mirror expansion

are to be modelled, which are illustrated in Fig. 13a. At a given location, in the vicinity of the flume's floor, the secondary fluorescence may be split into a component caused by direct irradiation from neighbouring primary fluorescence and a component caused by indirect fluorescence reflected by the glass floor. Further, there are two possible scenarios for this latter component dependent on the angle of incidence of this fluorescent light with the glass floor. If the incidence angle ψ is larger than the critical angle ψ_c (which is equal to 57° for a water-glass interface) then total internal reflection will occur. Alternatively, if ψ is smaller than ψ_c then regular reflection will take place at the glass floor according to the optical properties of the glass, which may be characterized by a reflection coefficient β. For standard glass it is usually assumed that approximately 95 % of the incident light is transmitted and 5 % is reflected and thus $\beta \simeq 0.05$.

Let us now consider the secondary fluorescence emitted by a particular point. The component caused by incident light that has been reflected from the wall is not considered in (16). It can be modelled in a similar fashion to the placement of image vortices when considering vortex dynamics in proximity to a solid boundary. The reflected light is modelled as direct illumination from an artificial source outside of the flume as illustrated in Fig. 13b. These artificial sources should be located symmetrically to the original emitter (where the floor defines the axis of symmetry), and their intensities need to be suitably scaled with the appropriate reflection coefficient (1 for total internal reflection and β for regular reflection). In the simplistic case, in which total internal reflection is not considered, modelling the reflection contribution is trivial, one simply fills zone V with the image reflected in the flume's floor and multiplied by the assumed β before applying (16). If, however, both reflection types are to be considered then (16) has to be updated to account for their different respective reflection coefficients. A detailed description of this complex approach is provided in "Appendix".

Having defined the methods of image extension, it is possible to approach the next step, i.e. defining an optimization procedure to evaluate the kernel's parameters. 50 B profiles that exhibit features similar to those presented in Fig. 11a (i.e. the smoothing effect is clearly identifiable), acquired at different camera's stations and time instants, were selected for the evaluation of $\hat{G}$ (examples are given in Fig. 14). Next, each of them was further truncated to ensure only an area over which $\tilde{B}$ should be uniform is considered (the area where no dye residence is expected). An example is highlighted with a dashed line in Fig. 14. Note that this procedure, at both profile selection stage and truncation stage, is somewhat arbitrary. Setting a feasible quantitative approach to identifying areas in which all the image non-uniformity is caused purely by the secondary fluorescence smoothing is, unfortunately, beyond the scope of the present study. Nevertheless, the arbitrariness is minimized, in an averaged sense, when a large number of profiles are considered. The optimization procedure is set to minimize a certain norm representative of the uniformity of the truncated $\tilde{B}$ profiles that results from applying (18) to the selected B profiles. There are a number of suitable uniformity measures that can be applied here. Let us arbitrarily

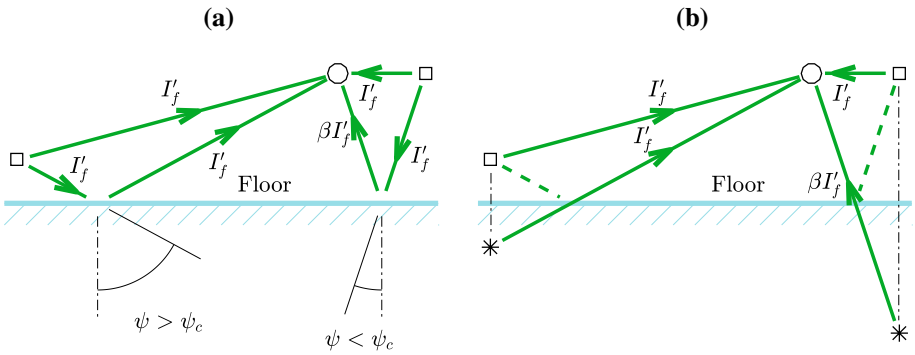

Fig. 13 Secondary illumination due to primary fluorescence in the vicinity of the floor (the *circle* represents the point of interest being irradiated by fluorescent light and the *square* represents the points emitting this fluorescent light). **a** The physical scenario: part of the incident light is transmitted directly and part is reflected by the floor, with the reflection coefficient β depending on the incidence angle ψ. **b** The proposed model: the reflections are replaced by direct transmission from artificial sources (*asterisks*) whose intensities are weighted by the appropriate reflection coefficient

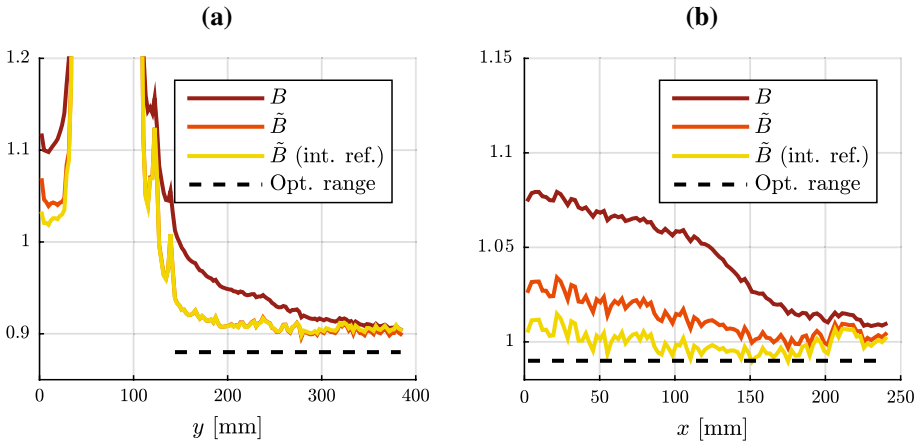

Fig. 14 Examples of B profiles utilized in the kernel evaluation versus the resolved $\tilde{B}$ profiles (both including and not including total internal refection) taken along: **a** the *vertical direction* and **b** the *horizontal direction* (the same profile is presented in Fig. 11); the dashed line indicates the imposed uniformity area

pick the L_2 norm of a vector formed by the slopes of linear least square fits to the resulting $\tilde{B}$ profiles. The optimization space is spanned by the kernel's parameters, where the exponent n is expected to fall into the interval $1 \leq n \leq 2$ based on the sphere-surface growth argument (the exponent value could be deviated towards 1 in the case of quasi-2D concentration fields for instance). The value of θ, which equals the kernel's integral, is assumed to be of order unity as it is linked to the share of the secondary fluorescence in the overall radiation.

The optimization procedure was performed for both expansion approaches. The solutions in both cases were very similar, i.e. the minimum of the considered norm appeared at a point $(\theta, n) = (1.5, 1.78)$ which is quite coherent with our former expectations. Evolution of the semi-optimized norm (optimized only for n) plotted as a function of θ, displayed in Fig. 15a along with the corresponding optimal n, illustrates the optimization space's topology. The resulting kernel's profile is given in Fig. 15b. The associated $\tilde{B}$ profiles, depicted in Fig. 14, present a significant improvement when compared to the original B profiles. Apart from approaching uniformity in the designated areas, they converge towards B as the distance from the dye puff (the peak in the profile) increases and reaches a value close to unity near the flume's floor ($y \simeq 0$ mm). The latter is particularly clear from Fig. 14b which shows the lower horizontal profile previously presented in Fig. 11. Both features seem physical, and neither of them was directly enforced during the optimization process which supports the proposed modelling technique. B and $\tilde{B}$ should collapse away from the c field's non-uniformity as when the ratio $\chi \cdot \chi_b^{-1}$ equals unity (uniform concentration fields are supposed to create identical χ fields) the definitions of B and $\tilde{B}$ are exactly the same. $\tilde{B}$ is expected to oscillate around 1 close to the flume's floor (only if the area is not occupied by a dye blob) which follows directly from (18) (as the attenuation can be neglected at $r \simeq r_0$).

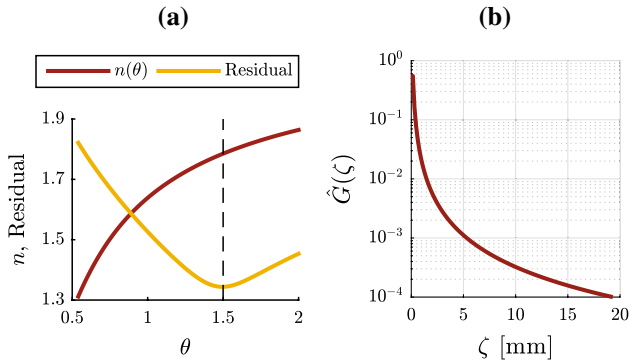

Fig. 15 Kernel evaluation results: **a** the semi-optimized uniformity norm (residual) and the corresponding optimal n evolutions, **b** the kernel's profile (note that the kernel is axisymmetric)

Regardless of the fact that both mirroring techniques (including and not including total internal reflection) result in fairly similar kernels, the produced $\tilde{B}$ profiles are not the same. It seems that although the range of the total internal reflection influence is limited to an area close to the floor (this is where the profiles differ most), it accounts for a considerable proportion of $\tilde{B}$. It is most clear in Fig. 14b where the profile is almost completely flattened once this effect is acknowledged. Nevertheless, the additional effort is rather high (see "Appendix") compared to the gain, and therefore, a simplistic approach is adopted from now on. However, an effective reflection rate is to be utilized which shall be equal to 0.8 to match the complex case as close as possible (this was established in an auxiliary study).

It is worth noting that values of the kernel's parameters are likely to change with the experimental conditions. Certainly, there is a dependence on the vessel's dimensions [this was shown by Vanderwel and Tavoularis (2014)] and shape (due to the expansion conditions). One can also easily imagine that the density of PIV seeding plays a certain role as well. Additionally, the exponent n reflects, to some extent, the topology of the characteristic concentration

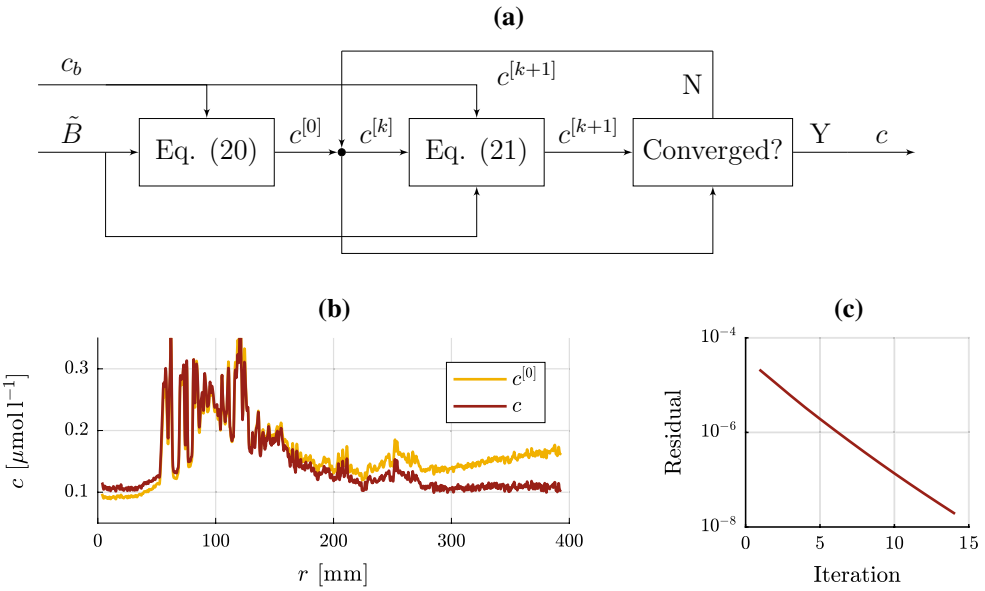

Fig. 16 **a** Block diagram of the normalized image $\tilde{B}$ quantification procedure, **b** an example of the initial and converged c profiles and **c** the loop's residual

structures, i.e. whether they are fully 3D or quasi-2D. Therefore, the obtained values of n and θ cannot simply be applied in an arbitrary experiment, but rather must be recalculated for each specific experimental setup. It is also worth mentioning that the proposed methodology for establishing values of the kernel's parameters is not suitable for the tank experiment as the smoothing effect of the secondary fluorescence cannot be distinguished in a case of uniform concentration field.

A MATLAB implementation of the described secondary fluorescence correction algorithm, along with its application to an example, is available for download at http://www.multisolve.eu/PLIF_Calib/.

4.3 Concentration field evaluation

Up until this point the manuscript has focused on the methodologies to evaluate the compensated image $\tilde{B}$. Therefore, it is suitable now to present an approach to solving (18) for the c field. Let us start by assigning some arbitrary initial guess to c_b, e.g. the lowest concentration value considered in the tank experiment. It should be possible now to integrate (18) numerically via a Runge–Kutta procedure, for instance; however, this would require a considerable amount of computational effort. Alternatively, one is able to solve (18) analytically, separately for each radial line, under an assumption that a functional form of the quantum yield ϕ can be expressed by (19), where a_k are the fit's parameters (equal to 0.239, 0.017, 0.465, respectively), instead of (13). Fortunately, it is possible to fit (19) into the observed ϕ evolution with a satisfactory level of accuracy (see Fig. 8). The associated analytical solution of (18) is given by (20). A trivial iterative procedure, defined by (21) (the block diagram is presented in Fig. 16a), can be further utilized to account for the discrepancy between the ϕ given by (19) and the one provided in (13) [i.e. the $\phi(c)$ function that appears in (21) should be understood in terms of (13)], as the latter represents the measurements much better, especially at low values of c. The procedure reaches convergence within several iterations, as shown in Fig. 16c. An example of a comparison between the initial and the converged solution is presented in Fig. 16b.

$$\phi(c)\cdot{\phi_\mathrm{max}}^{-1} \simeq \frac{a_1(c-a_2)^{a_3}}{c} \tag{19}$$

$$c(r,\alpha) = a_2 - \frac{a_3}{\epsilon}\frac{\mathrm{d}}{\mathrm{d}r} \times \log\left(1 - \frac{\epsilon}{a_3}\int_{r_0}^{r} \sqrt[a_3]{\frac{\tilde{B}(r,\alpha)\phi(c_\mathrm{b})c_\mathrm{b}}{a_1}}\exp\left(\frac{\epsilon a_2 r}{a_3}\right)\mathrm{d}\zeta\right) \tag{20}$$

$$c^{[k+1]}(r,\alpha) = \frac{\tilde{B}(r,\alpha)\phi(c_\mathrm{b})c_\mathrm{b}}{\phi(c^{[k]}(r,\alpha))} \times \exp\left(-\epsilon\int_{r_0}^{r}\left(c^{[k]}(\zeta,\alpha)-c_\mathrm{b}\right)\mathrm{d}\zeta\right)^{-1} \tag{21}$$

The only remaining issue is the background concentration c_b. In order to address it, let us consider a scenario, where a dye puff is confined in the centre of an image and there is only background dye level residing near to the image's upper and lower edge. It is relatively easy to find several such images within an acquired set. The quantification procedure described above would only return the same value at the top and bottom of the image, if the correct c_b was assumed. Otherwise there would be a discrepancy

between the two edges, as a wrong value of c_b results in under- or overestimation of the light attenuation. Therefore, it is possible to establish the correct c_b by searching for the value that matches the obtained concentration result at these locations. It is important to note that this needs to be done just once per measurement set (although it is worth averaging c_b over several calculations), so the procedure does not introduce any serious computational effort.

5 Application to the main experiment

Let us now review some example results to assess how the secondary fluorescence affects a PLIF measurement. It is first possible to quantify its share in the overall fluorescence which is gathered by the $1 - \chi$ field. The background images contain the uniformly distributed secondary fluorescence whose mean value oscillates around 67 % with a standard deviation of 0.9 %. It is worth noting that based on (16) and (17) one could come up with an approximation of the mean secondary fluorescence share gathered by $\theta(1+\theta)^{-1}$, which gives a reasonable estimate of 60 % (the secondary fluorescence scales with the kernel's integral θ and the total fluorescence scales with $1+\theta$, which in turn leads to the aforementioned simplified approximation of their ratio). The empirical correlation formula (15) applied to the flume case (the flume width is taken as the input) returns a value of 52 %, which is a bit less; however, one needs to bear in mind that the formula was prepared for a relatively small tank (see Vanderwel and Tavoularis 2014), and therefore, the lower value is justified. Nevertheless, these two values are comparable.

On the other hand, the secondary fluorescence contribution was non-uniform for the main experiment's images (a typical example is depicted in Fig. 17). The value ranged from 50 % to 90 %; however, the mean was only slightly higher than in the previous case reaching roughly 68 %. Typically a decreased level of the secondary fluorescence is observed at the bright spots, i.e. where the local concentration value is high. Similar behaviour was noted by Vanderwel in the tank experiment (the information was shared via private communication) who observed a higher secondary fluorescence level at the periphery of the laser sheet compared to the one reached at its centre. This behaviour can be justified by simple logic, i.e. the locally brightest points benefit from the secondary illumination that comes from the relatively darker spots only, whereas a dark point can be illuminated by the brighter ones if located sufficiently close.

Figure 18 presents a comparison between an example normalized image B and the corresponding image $\tilde{B}$

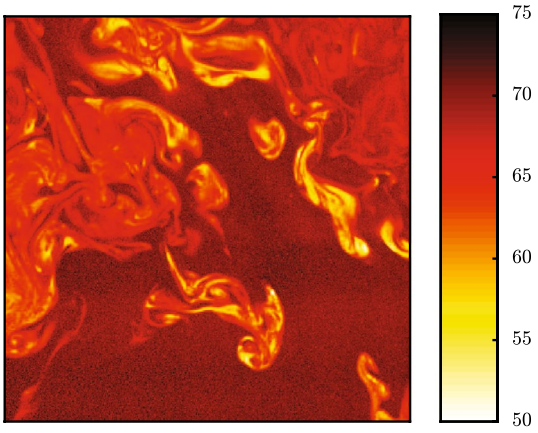

Fig. 17 An example of the instantaneous percentage share of the secondary fluorescence in the overall fluorescence

(compensated for the secondary fluorescence effect). It follows from the PDF that the latter exhibits a wider observation range (i.e. B underrepresents the high values). Additionally, the peak, which should be ideally located at 1 as it corresponds to the background fluorescence level, is shifted back towards 1 in the case of $\tilde{B}$ because the dye puff's glare is removed. The power spectral density (PSD) shows a relatively higher content of low wave numbers in the B case which has to do with a blurring effect of the secondary fluorescence. Since a deconvolution procedure is used to recover $\tilde{B}$, the noise level is increased in this case, which is clearly marked in both the PSD and the PDF. A visual inspection of the actual images (Fig. 18a, b) confirms all the aforementioned observations.

The background concentration level, evaluated separately for each measurement station, oscillated around $0.8\,\mu\mathrm{mol\,l}^{-1}$, which roughly resulted in 16 % of the incident laser light being attenuated during its transit through the field of view. This effect is compensated by normalizing the original images H with the background image H_b [see (9)]. However, additional attenuation that arises from the dye plume presence adds to that and needs to be considered via (21). It turned out that this effect caused up to 20 % of additional attenuation throughout the measurement's course (i.e. up to 36 % of the initial illumination energy was absorbed by the dye within the field of view). A typical instantaneous example of the additional attenuation is presented in Fig. 19 along with the corresponding normalized concentration field. It is also worth noting that the additional attenuation introduces an error that convects with the flow, as the shadow behind a concentrated blob of dye moves concurrently with the blob (see Fig. 20), which is likely to alter the measured dynamical properties of the concentration field as well as the spatial correlations.

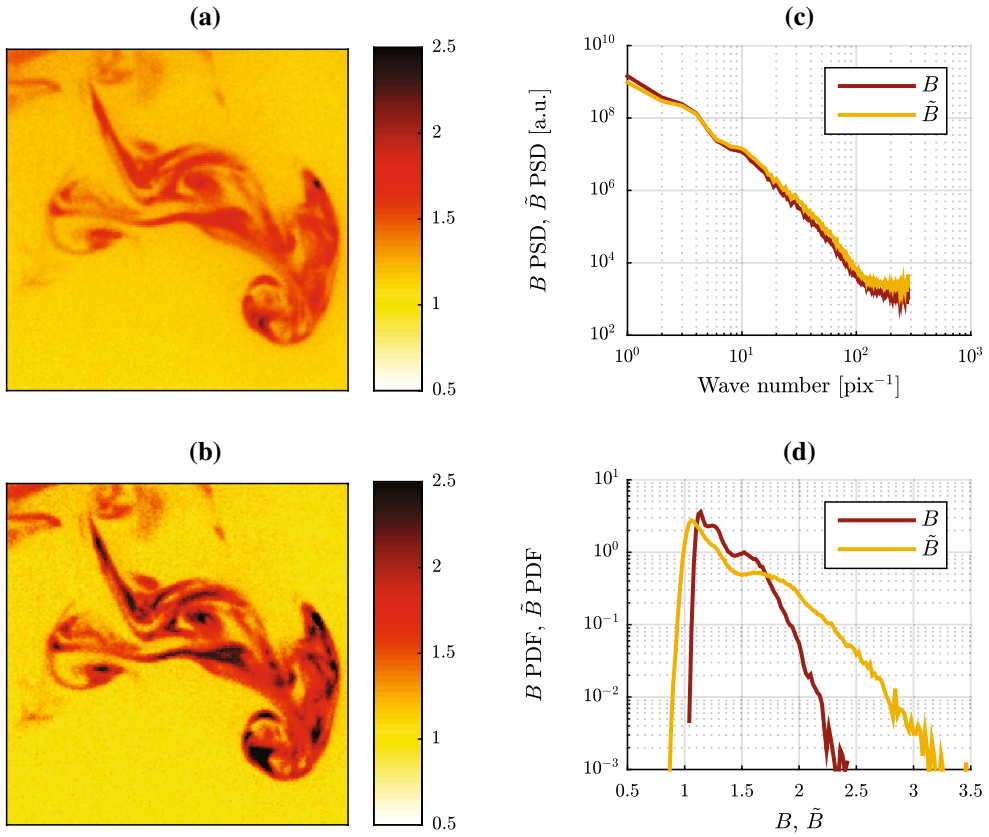

Fig. 18 Examples of normalized images **a** B and **b** $\tilde{B}$, along with their characteristics: **c** power spectral density functions and **d** histograms

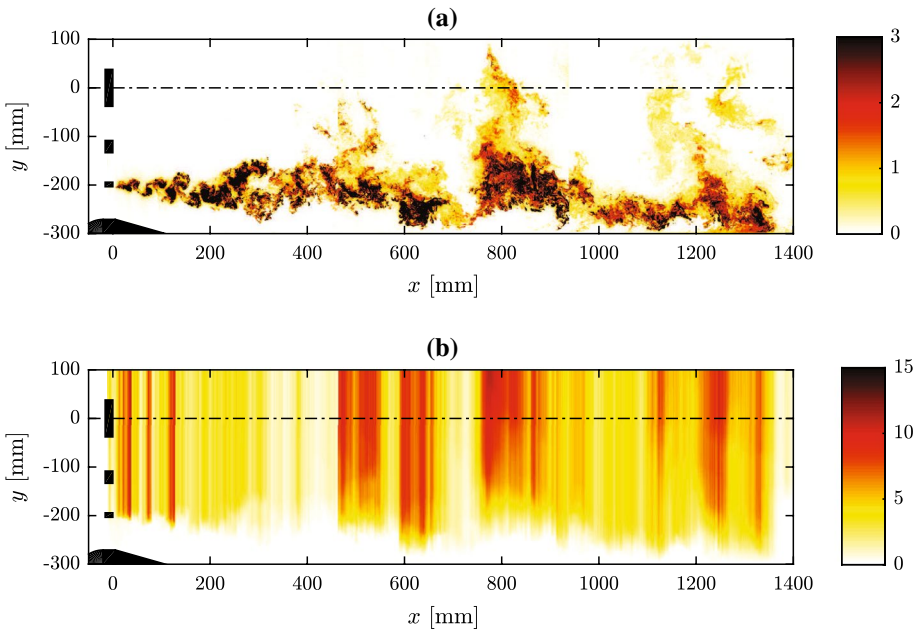

Fig. 19 **a** Instantaneous concentration fields (data acquired at stations X_1, X_2 and X_3) normalized with a local c transverse profile's standard deviation and **b** the corresponding percentage laser light attenuation

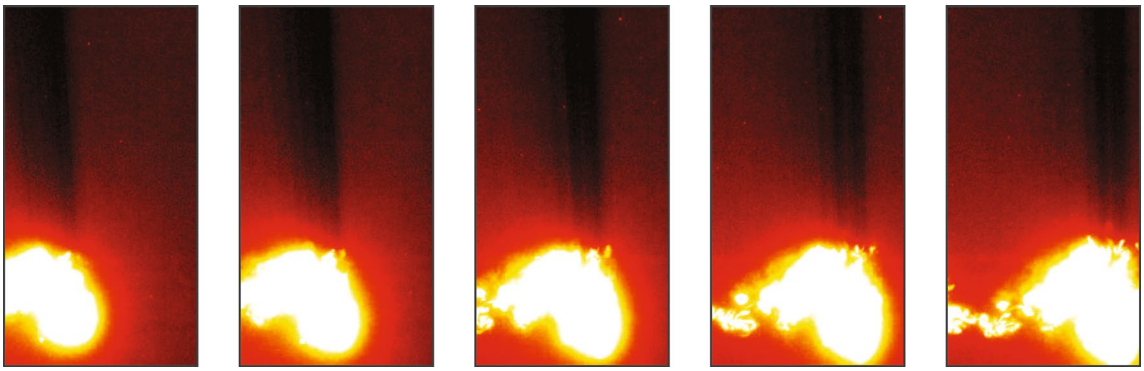

Fig. 20 A sequence of *B* images; the absorption shadows are convected with the flow

6 Conclusions

It is shown that the effects of secondary fluorescence can have a significant influence on the quantification of PLIF images if it is not specifically accounted for in the calibration procedure. In the main experiment of the current manuscript it was shown that the secondary fluorescences share of the total acquired signal exceeded 50 %, which is in agreement with the values reported in Vanderwel and Tavoularis (2014). This level depends on several factors including the size of the experimental facility and the spatial topology of the scalar field. The relative level of secondary fluorescence is found to be lower in localized "blobs" of high concentration and reaches its maximum value in the ambient regions of the flow. The result of this secondary fluorescence is to reduce the depth of scalar field that can be recorded. Further, it introduces a smoothing effect which may be mistaken for diffusion despite the generally high Schmidt numbers that are used for typical PLIF dyes, such as rhodamine 6G, in water.

In addition to secondary fluorescence, it is shown that the attenuation of the incident light by localized patches of high concentration within the scalar field can also lead to significant calibration errors (up to 36 % of the incident laser light was attenuated in the main experiment considered in this manuscript). The instantaneous attenuation distribution manifests as "shadow" regions, aligned with the incident light rays and positioned above these local "blobs" of high concentration (in the sense of travel of the light ray) that convect with the flow. Note that in a shear flow, such as the one considered in the main experiment of this manuscript, these convection velocities will vary with the cross-stream location of the high concentration "blobs". It is possibly also worth pointing out that their convection velocities may vary according to their characteristic length-scale too, as shown by Buxton et al. (2013). This attenuation can alter the statistical moments of the acquired data in addition to its dynamical properties. It is not possible to account for this phenomenon with a traditional, pixel-by-pixel calibration approach.

This manuscript introduces a new calibration procedure that is well adapted to account for these potential error sources. This is made possible by considering the concentration dependence of the quantum yield of the fluorescence, as well as the illumination's attenuation, gathered by Eq. (18). This makes the proposed calibration method a suitable tool for high concentration PLIF measurements in which the Beer–Lambert law cannot be assumed to be a linear function. Such high concentration PLIF measurements are required if a high dynamic range of concentrations are to be measured, for example if one wishes to evaluate the spatial evolution of a scalar field along a large spatial extent. At the same time, the proposed method accounts for the secondary fluorescence, which has been recently recognized by Vanderwel and Tavoularis (2014) as an important error source, through careful modelling of the underlying physics. Last but not least, the designed calibration method is numerically efficient since the most expensive task, solving Eq. (18), exploits an analytical approximation to the solution to produce a realistic starting point to the iterative procedure. The proposed technique thus contributes a significant advancement to the quantification of PLIF experiments to measure scalar concentrations in fluid flows.

Acknowledgments The authors acknowledge support from the EU through the FP7 Marie Curie MULTISOLVE project (Grant Agreement No. 317269).

Open Access This article is distributed under the terms of the Creative Commons Attribution 4.0 International License (http://creativecommons.org/licenses/by/4.0/), which permits unrestricted use, distribution, and reproduction in any medium, provided you give appropriate credit to the original author(s) and the source, provide a link to the Creative Commons license, and indicate if changes were made.

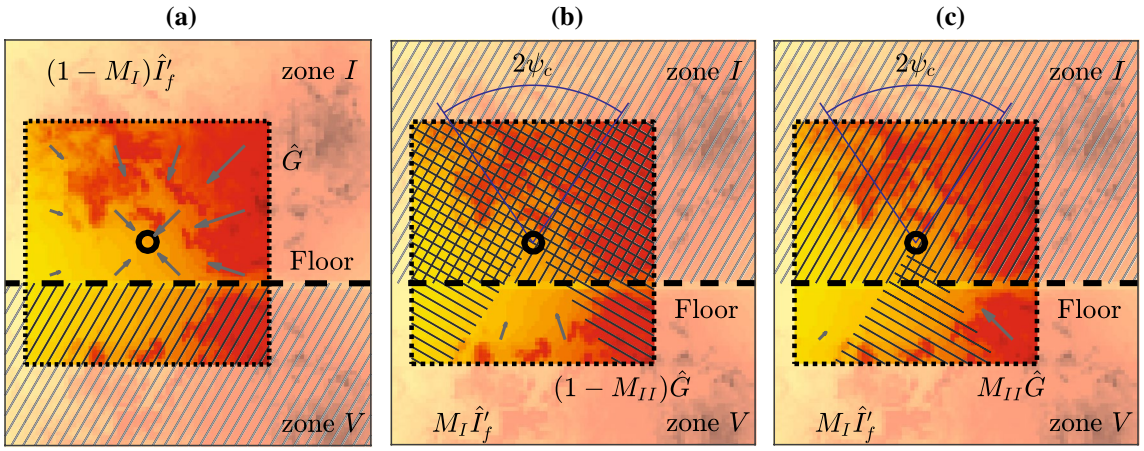

Fig. 21 Schematic illustrating evaluation of the secondary fluorescence components at a given point (represented by the *circle*) in the vicinity of the floor. The *dotted box* represents the kernel's extent, and the *hatched areas* indicate the adopted masks. **a** $\left((1-M_I)\hat{I}'_{\mathrm{f}}\right) * \hat{G}$—the direct illumination part. **b** $\left(M_I\hat{I}'_{\mathrm{f}}\right) * \left((1-M_{\mathrm{II}})\hat{G}\right)$—the regular reflection part. **c** $\beta^{-1}\left(M_I\hat{I}'_{\mathrm{f}}\right) * \left(M_{\mathrm{II}}\hat{G}\right)$—the total internal reflection part

Appendix: The complex mirror expansion: inclusion of total internal reflection

The simplistic mirror expansion technique accounts only for regular reflection. In order to additionally acknowledge total internal reflection in the compensated image $\tilde{B}$ evaluation procedure one needs to update Eq. (16). For this reason let us examine the expression for the secondary fluorescence, $\hat{I}'_{\mathrm{f}} * \hat{G}$, assuming that zone V (see Fig. 12) is filled in exactly the same manner as in the simplistic case (i.e. it is filled with the image reflected in the flume's floor and multiplied by the assumed reflection coefficient β). It follows from the distributivity of the convolution operator $(A * (B + C) \equiv A * B + A * C$ for general matrices A, B and C) that this may be equivalently written as $\left(M_I\hat{I}'_{\mathrm{f}}\right) * \hat{G} + \left((1-M_I)\hat{I}'_{\mathrm{f}}\right) * \hat{G}$. In this expression M_I is a masking matrix equal to 0 everywhere except for zone V. The two terms represent the reflection and the direct illumination contributions to the secondary fluorescence, respectively (see Fig. 21 for illustration). The first term can be further split into $\left(M_I\hat{I}'_{\mathrm{f}}\right) * \left((1-M_{\mathrm{II}})\hat{G}\right)$ and $\left(M_I\hat{I}'_{\mathrm{f}}\right) * \left(M_{\mathrm{II}}\hat{G}\right)$, where M_{II} is another masking matrix that blocks influence from angular positions at which regular reflection occurs, i.e. where the incidence angle is smaller than the critical angle ψ_{c}. These two components may therefore be considered to represent the share of regular and total internal reflection, except the latter needs to be compensated for its apparent reflection coefficient. Note that the factor of β is already embedded in the extended image (so regular reflection is represented correctly) and thus one needs to multiply the second term by β^{-1} to ensure the total internal reflection's coefficient equals 1. The total secondary fluorescence may now be computed by summing all these terms. It is simple to show that (22) is reached as the final result, which contains an additional term in comparison with (16).

$$\begin{aligned} h^{-1}\left(H(x,y)\right) \simeq \mathrm{Const}\cdot\Big(&\hat{I}'_{\mathrm{f}}(x,y) * \left(\delta(x,y) + \hat{G}(x,y)\right) \\ &+ \beta^{-1}(1-\beta)\left(M_I(x,y)\hat{I}'_{\mathrm{f}}(x,y)\right) \\ &* \left(M_{\mathrm{II}}(x,y)\hat{G}(x,y)\right)\Big) \\ \mathcal{F}\left\{h^{-1}\left(H\right)\right\} = \mathrm{Const}\cdot\Big(&\mathcal{F}\{\hat{I}'_{\mathrm{f}}\}\mathcal{F}\{\delta+\hat{G}\} \\ &+ \beta^{-1}(1-\beta)\left(\mathcal{F}\{M_I\} * \mathcal{F}\{\hat{I}'_{\mathrm{f}}\}\right)\mathcal{F}\{M_{\mathrm{II}}\hat{G}\}\Big) \end{aligned} \tag{22}$$

Equation (22) cannot be solved for $\hat{I}'_{\mathrm{f}}$ as simply as (16) and requires considerable computational effort. One needs to note that the convolution theorem for continuous signals does not apply directly to discrete ones, i.e. the Fourier transform of a product of two continuous signals equals the convolution of their transforms, whereas the *FFT* of a product translates to the circular convolution of the two discrete signals divided by its length. Therefore, the following solution technique applies to discrete data only.

Each of the fields involved in (22) is represented by a matrix of size $N_y \times N_x$. It is generally possible to express the problem of establishing $\mathcal{F}\{\hat{I}'_{\mathrm{f}}\}$ (which conveniently links to $\hat{I}'_{\mathrm{f}}$ thorough the inverse Fourier transform) as a linear system of size $N_xN_y \times N_xN_y$, which is rather challenging given the resolution of the images. Fortunately, since M_I is purely a function of the y coordinate (i.e. M_I only varies along the vertical direction), one can decouple this problem into N_x tasks of size $N_y \times N_y$, where each represents evaluating a single vertical line of $\mathcal{F}\{\hat{I}'_{\mathrm{f}}\}$. The solution procedure, for the particular line denoted by i_x^0, is gathered by (23) (i_x and i_y

are the matrices' indices and k is an integer). Note that an unitalicized font is used to indicate the numerical representation of discussed field quantities.

$$\begin{aligned}\mathrm{Const}\cdot\mathcal{F}\{\hat{\mathrm{I}}_{\mathrm{f}}'\}[i_y,i_x^0] &= \mathrm{A}^{-1}\cdot\mathcal{F}\left\{h^{-1}\left(\mathrm{H}\right)\right\}[i_y,i_x^0]\\ \mathrm{A}[i_y,i_x] &= \mathrm{diag}\left(\mathcal{F}\{\delta+\hat{\mathrm{G}}\}[i_y,i_x^0]\right)\\ &\quad+(1-\beta)\cdot A_0\cdot\mathrm{diag}\left(\mathcal{F}\{\mathrm{M_{II}}\hat{\mathrm{G}}\}[i_y,i_x^0]\right)\\ \mathrm{A}_0[i_y,i_x] &= N_y^{-1}\mathcal{F}\{\mathrm{M_I}\}[i_x-i_y+kN_y,1]\end{aligned}\tag{23}$$

References

Bindhu C, Harilal S, Nampoori V, Vallabhan C (1999) Solvent effect on absolute fluorescence quantum yield of rhodamine 6G determined using transient thermal lens technique. Mod Phys Lett B 13(16):563–576

Buxton O, de Kat R, Ganapathisubramani B (2013) The convection of large and intermediate scale fluctuations in a turbulent mixing layer. Phys Fluids 25(12):125105

Crimaldi J (1997) The effect of photobleaching and velocity fluctuations on single-point LIF measurements. Exp Fluids 23(4):325–330

Crimaldi J (2008) Planar laser induced fluorescence in aqueous flows. Exp Fluids 44(6):851–863

Deusch S, Dracos T (2001) Time resolved 3D passive scalar concentration-field imaging by laser induced fluorescence (LIF) in moving liquids. Meas Sci Technol 12(2):188

Ferrier A, Funk D, Roberts P (1993) Application of optical techniques to the study of plumes in stratified fluids. Dyn Atmos Oceans 20(1):155–183

Gendron P, Avaltroni F, Wilkinson K (2008) Diffusion coefficients of several rhodamine derivatives as determined by pulsed field gradient-nuclear magnetic resonance and fluorescence correlation spectroscopy. J Fluoresc 18(6):1093–1101

Hannoun IA, List EJ (1988) Turbulent mixing at a shear-free density interface. J Fluid Mech 189:211–234

Koochesfahani M, Dimotakis P (1985) Laser-induced fluorescence measurements of mixed fluid concentration in a liquid plane shear layer. AIAA J 23(11):1700–1707

Laizet S, Vassilicos J (2012) Fractal space-scale unfolding mechanism for energy-efficient turbulent mixing. Phys Rev E 86(4):046302

Penzkofer A, Lu Y (1986) Fluorescence quenching of rhodamine 6G in methanol at high concentration. Chem Phys 103(2):399–405

Penzkofer A, Leupacher W (1987) Fluorescence behaviour of highly concentrated rhodamine 6G solutions. J Lumin 37(2):61–72

Sarathi P, Gurka R, Kopp GA, Sullivan PJ (2012) A calibration scheme for quantitative concentration measurements using simultaneous PIV and PLIF. Exp Fluids 52(1):247–259

Selwyn JE, Steinfeld JI (1972) Aggregation of equilibriums of xanthene dyes. J Phys Chem 76(5):762–774

Shan JW, Lang DB, Dimotakis PE (2004) Scalar concentration measurements in liquid-phase flows with pulsed lasers. Exp Fluids 36(2):268–273

Vanderwel C, Tavoularis S (2014) On the accuracy of PLIF measurements in slender plumes. Exp Fluids 55(8):1–16

Walker D (1987) A fluorescence technique for measurement of concentration in mixing liquids. J Phys E Sci Instrum 20(2):217

Zhu Y, Mullins OC (1992) Temperature dependence of fluorescence of crude oils and related compounds. Energy Fuels 6(5):545–552